to 78% yield). Many aryl bromides function effectively as well, including those that contain functional groups as diverse as ketones, esters, nitriles, trifluoromethyl groups, and fluorides (**14** to **18**, 75 to 90% yield). Heteroaromatics, in the form of differentially substituted bromopyridines, are also efficient coupling partners (**19** to **22**, 60 to 85% yield). Moreover, aryl chlorides are competent substrates if the arenes, such as pyridines and pyrimidines, are electron-deficient (**23** and **24**, 64 and 65% yield). Only products **15** and **19** in Fig. 3 would be accessible by using our previously reported photoredox arylation strategy. Moreover, we are unaware of the general use of C_{sp^3}-bearing carboxylic acids as reaction substrates in transition metal catalysis, an illustration of the tremendous scope expansion that is attainable by using this dual catalysis technology. These reactions are typically complete in 72 hours at larger scale and 48 hours on smaller scale (see supplementary text).

Next, we investigated the nature of the carboxylic acid coupling partner, as highlighted in Fig. 4A. A wide variety of α-amino acids function effectively in this protocol, including various *N*-Boc and *N*-benzyl carbamoyl (*N*-Cbz) protected heterocycles (**25** to **27**, 61 to 93% yield). Acyclic α-amino acids, containing indole, ester, and thioether functionalities, are also readily tolerated (**28** to **32**, 72 to 91% yield). α-oxycarboxylic acids can function as proficient coupling partners, producing α-arylated ethers in high yield over a single step (**33**, 82% yield). Moreover, we have also found that various phenyl acetic acid substrates function in this coupling protocol with high efficiency (>78% yield, see supplementary text).

To further demonstrate the utility of this dual-catalysis strategy, we sought to demonstrate the direct functionalization of C_{sp^3}–H bonds with coupling partners derived from aryl or alkyl halides. Given that our decarboxylation-arylation mechanism involves the rapid addition of an α-amino radical to a Ni(II) salt, we sought to generate an analogous α-nitrogen carbon–centered radical via a photoredox-driven *N*-phenyl (*N*-Ph) oxidation, α-C–H deprotonation sequence using aniline-based substrates (*18*). We presumed that this photomediated *N*-Ph oxidation mechanism would provide an alternative pathway to the open-shell carbon intermediate (corresponding to **4**, Fig. 2) and should similarly intercept the putative Ni(II) intermediate **8**. Assuming that the remaining dual-catalysis mechanism would be analogous to that shown in Fig. 2, we expected that a range of direct C_{sp^3}–H functionalization protocols should be possible. Indeed, we were able to demonstrate that dimethylaniline undergoes α-amine coupling with a variety of aryl halides in the presence of $Ir[dF(CF_3)ppy]_2(dtbbpy)PF_6$ and $NiCl_2$•glyme (Fig. 4B). Electron-deficient and electron-rich iodoarenes give moderate to high yields (**34** to **36**, 72 to 93% yield). Moreover, aryl bromides are competent coupling partners, enabling the installation of medicinally important heterocyclic motifs (**37**, 60% yield). Last, control experiments have revealed that the combination of light, photoredox catalyst **1**, and the $NiCl_2$•dtbbpy complex is essential for product formation in all examples listed in Figs. 3 and 4. This reaction represents a powerful foray into direct C–H activation using orthogonal cross-coupling reactivity.

REFERENCES AND NOTES

1. D. A. Nicewicz, D. W. C. MacMillan, *Science* **322**, 77–80 (2008).
2. M. A. Ischay, M. E. Anzovino, J. Du, T. P. Yoon, *J. Am. Chem. Soc.* **130**, 12886–12887 (2008).
3. J. M. R. Narayanam, J. W. Tucker, C. R. J. Stephenson, *J. Am. Chem. Soc.* **131**, 8756–8757 (2009).
4. D. S. Hamilton, D. A. Nicewicz, *J. Am. Chem. Soc.* **134**, 18577–18580 (2012).
5. M. T. Pirnot, D. A. Rankic, D. B. C. Martin, D. W. C. MacMillan, *Science* **339**, 1593–1596 (2013).
6. M. R. Netherton, G. C. Fu, *Adv. Synth. Catal.* **346**, 1525–1532 (2004).
7. A. Rudolph, M. Lautens, *Angew. Chem. Int. Ed.* **48**, 2656–2670 (2009).
8. The successful merger of photoredox and transition metal catalysis has been demonstrated for the specific installation of unique functionality (e.g., CF_3) (*9*–*14*).
9. M. Osawa, H. Nagai, M. Akita, *Dalton Trans.* **2007**, 827–829 (2007).
10. D. Kalyani, K. B. McMurtrey, S. R. Neufeldt, M. S. Sanford, *J. Am. Chem. Soc.* **133**, 18566–18569 (2011).
11. Y. Ye, M. S. Sanford, *J. Am. Chem. Soc.* **134**, 9034–9037 (2012).
12. M. Rueping *et al.*, *Chemistry* **18**, 5170–5174 (2012).
13. B. Sahoo, M. N. Hopkinson, F. Glorius, *J. Am. Chem. Soc.* **135**, 5505–5508 (2013).
14. X. Z. Shu, M. Zhang, Y. He, H. Frei, F. D. Toste, *J. Am. Chem. Soc.* **136**, 5844–5847 (2014).
15. S. Biswas, D. J. Weix, *J. Am. Chem. Soc.* **135**, 16192–16197 (2013).
16. S. L. Zultanski, G. C. Fu, *J. Am. Chem. Soc.* **135**, 624–627 (2013).
17. Z. Zuo, D. W. C. MacMillan, *J. Am. Chem. Soc.* **136**, 5257–5260 (2014).
18. A. McNally, C. K. Prier, D. W. C. MacMillan, *Science* **334**, 1114–1117 (2011).
19. T. J. A. Graham, J. D. Shields, A. G. Doyle, *Chem. Sci.* **2**, 980 (2011).
20. K. T. Sylvester, K. Wu, A. G. Doyle, *J. Am. Chem. Soc.* **134**, 16967–16970 (2012).
21. J. D. Shields, D. T. Ahneman, T. J. A. Graham, A. G. Doyle, *Org. Lett.* **16**, 142–145 (2014).
22. M. S. Lowry *et al.*, *Chem. Mater.* **17**, 5712–5719 (2005).
23. M. Durandetti, M. Devaud, J. Perichon, *New J. Chem.* **20**, 659 (1996).
24. Y. H. Budnikova, J. Perichon, D. G. Yakhvarov, Y. M. Kargin, O. G. Sinyashin, *J. Organomet. Chem.* **630**, 185–192 (2001).
25. C. Amatore, A. Jutand, *Organometallics* **7**, 2203–2214 (1988).

ACKNOWLEDGMENTS

The authors are grateful for financial support provided by the NIH General Medical Sciences (grants NIHGMS R01 GM103558-01 and R01 GM100985-01) and gifts from Merck, Amgen, Eli Lilly, and Roche. Z.Z. and L.C. are grateful for postdoctoral fellowships from the Shanghai Institute of Organic Chemistry. The authors thank G. Molander and co-workers for graciously offering to concurrently publish a related study that was submitted slightly ahead of our own.

SUPPLEMENTARY MATERIALS

www.sciencemag.org/content/345/6195/437/suppl/DC1
Material and Methods
Supplementary Text
Tables S1 and S2
Data
References (*26*–*34*)

1 May 2014; accepted 27 May 2014
Published online 5 June 2014;
10.1126/science.1255525

EXOPLANET DETECTION

Stellar activity masquerading as planets in the habitable zone of the M dwarf Gliese 581

Paul Robertson,[1,2]* Suvrath Mahadevan,[1,2,3] Michael Endl,[4] Arpita Roy[1,2,3]

The M dwarf star Gliese 581 is believed to host four planets, including one (GJ 581d) near the habitable zone that could possibly support liquid water on its surface if it is a rocky planet. The detection of another habitable-zone planet—GJ 581g—is disputed, as its significance depends on the eccentricity assumed for d. Analyzing stellar activity using the Hα line, we measure a stellar rotation period of 130 ± 2 days and a correlation for Hα modulation with radial velocity. Correcting for activity greatly diminishes the signal of GJ 581d (to 1.5 standard deviations) while significantly boosting the signals of the other known super-Earth planets. GJ 581d does not exist, but is an artifact of stellar activity which, when incompletely corrected, causes the false detection of planet g.

At a distance of 6.3 parsecs, the M dwarf star Gliese 581 (GJ 581) is believed to host a system of planets discovered using the Doppler radial velocity (RV) technique (*1*–*3*) and a debris disk (*4*). It is considered a local analog to compact M dwarf planetary systems found by the Kepler spacecraft (*5*, *6*).

Although the periods and orbital parameters of the inner planets b (P = 5.36 days) and c (P = 12.91 days) are unchanged since their initial discovery (*1*, *2*), the period of planet d was revised from 82 to 66 days (*2*, *3*) upon the discovery of a fourth planet e (P = 3.15 days). Using a combination of data from the High Accuracy Radial Velocity Planet Searcher (HARPS) spectrograph and the High Resolution Echelle Spectrometer (HIRES), planets f (P = 433 days) and g (P = 36.5 days) were reported (*7*), and their existence promptly questioned (*8*) using additional data from HARPS. Although the reported

the α-amino radical **4** and the corresponding Ir^{II} species **5**. Given the established oxidation potential of prototypical amino acid carboxylate salts, we expected this process to be thermodynamically favorable [*tert*-butyl carbamoyl (Boc)–ProOCs, $E_{1/2}^{red}$ = +0.95 V versus SCE in CH_3CN) (*17*). Concurrently with this photoredox cycle, we hoped that oxidative addition of the Ni(0) species **6** into an aryl halide would produce the Ni(II) intermediate **7**. We anticipated that this Ni(II)-aryl species would rapidly intercept the α-amino radical **4**, forming the organometallic Ni(III) adduct **8**. Subsequent reductive elimination would forge the requisite C–C bond while delivering the desired α-amino arylation product **10** and expelling the Ni(I) intermediate **9**. Last, SET between the Ir^{II} species **5** and the Ni complex **9** would accomplish the exergonic reduction of Ni(I) to Ni(0) {on the basis of the established two-electron reduction potential of Ni(II) to Ni(0), we presume that reduction of Ni(I) to Ni(0) should be thermodynamically favorable, $E_{1/2}^{red}$ [Ni^{II}/Ni^{0}] = –1.2 V versus SCE in *N*,*N*′-dimethylformamide (DMF)} by the Ir^{II} species **5** {$E_{1/2}^{red}$ [Ir^{III}/Ir^{II}] = –1.37 V versus SCE in CH_3CN} (*22*, *23*), thereby completing both the photoredox and the nickel catalytic cycles simultaneously.

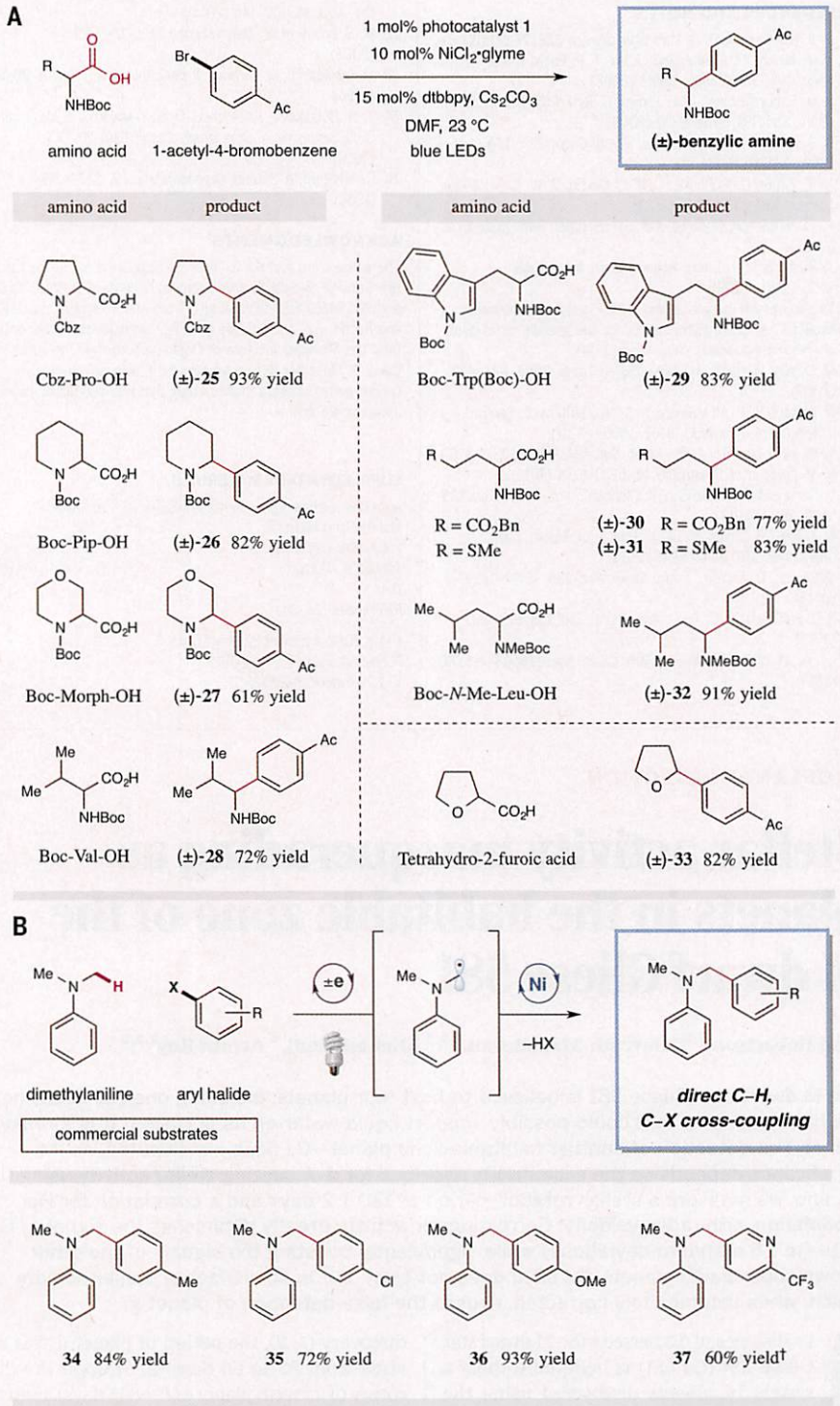

Fig. 4. Amino acid coupling partners and C_{sp^3}–H, C–X cross-coupling. (**A**) Evaluation of the amino acid coupling partner in the decarboxylative-arylation protocol. Ac, acetyl group; LED, light-emitting diode. (**B**) The direct C_{sp^3}–H, C–X cross-coupling via photoredox-nickel catalysis. All yields listed in Figs. 3 and 4 are isolated yields. Reaction conditions for (A) are the same as in Fig. 3. Reaction conditions for (B) are as follows: photocatalyst **1** [1 mole % (mol %)]; $NiCl_2$·glyme (10 mol %), dtbbpy (15 mol %), KOH (3 equiv.), DMF, 23°C, 26-W light. *Iodoarenes used as aryl halide, X = I. †Bromoarene used, X = Br.

With this mechanistic hypothesis in hand, we first examined the proposed coupling by using *N*-Boc proline, *para*-iodotoluene, and a wide range of photoredox and ligated nickel catalysts. To our delight, we found that the combination of Ir[dF(CF_3)ppy]$_2$(dtbbpy)PF_6 and $NiCl_2$•glyme (glycol ether), dtbbpy, in the presence of 1.5 equivalents of Cs_2CO_3 base and white light from a 26-W compact fluorescent bulb, achieved the desired fragment coupling in 78% yield. During our optimization studies, we found that use of a bench-stable Ni(II) source, such as $NiCl_2$•glyme, was sufficient to generate the arylation product with comparable efficiency to a Ni(0) source. We attribute this result to in situ photocatalytic reduction of Ni(II) to Ni(0) via two discrete SET events, with excess amino acid likely serving as the sacrificial reductant to access the active Ni catalyst {$E_{1/2}^{red}$ [Ni^{II}/Ni^{0}] = –1.2 V versus SCE in DMF} (*23*). We believe that it is unlikely that the Ni(II)(Ar)X intermediate **7** undergoes a SET event to form Ni(I)Ar, given the poorly matched reduction potentials of the species involved {compare with $E_{1/2}^{red}$ [$Ni^{II}ArX/Ni^{I}Ar$] = –1.7 V versus SCE in CH_3CN and $E_{1/2}^{red}$ [Ir^{III}/Ir^{II}] = –1.37 V versus SCE in CH_3CN} (*22*, *24*). However, we recognize that an alternative pathway could be operable wherein the oxidative addition step occurs from the Ni(I) complex to form a Ni(III) aryl halide adduct. In this pathway, photocatalyst-mediated reduction of the aryl-Ni(III) salt to the corresponding Ni(II) species followed by the α-amino radical addition step would then form the same productive Ni(III) adduct **8**, as shown in Fig. 2. Given that (i) Ni(0) complexes undergo oxidative addition more readily than Ni(I) complexes with aryl halides (*25*) and (ii) Ni(II) complexes are believed to rapidly engage with sp^3 carbon-centered radicals to form Ni(III) species (enabling sp^3–sp^2 and sp^3–sp^3 C–C bond formations) (*15*, *16*), we favor the dual-catalysis mechanism outlined in Fig. 2.

Having established the optimal conditions for this photoredox-nickel decarboxylative arylation, we focused our attention on the scope of the aryl halide fragment. As shown in Fig. 3, a wide range of aryl iodides are amenable to this dual-catalysis strategy, including both electron-rich and electron-deficient arenes (**10** to **13**, *65*

planet f is now believed not to exist, the existence of planet g is still claimed by some groups. Vogt *et al.* (*9*) argue for a five-planet circular model (including g) based on dynamical stability, whereas studies based on Bayesian statistics (*10*) and correlated noise (*11*, *12*) find no evidence for the existence of g. At close to half the period of d, its RV signal strongly depends on the eccentricity assumed for the fit to planet d (*9*, *13*). The existence of planet d itself has been questioned; an analysis using a correlated noise model (*11*) reduced its significance to 2 SD, although d is still widely believed to exist by the astronomy community. The Gliese 581 system is also of great interest because three of the planets (c, d, and g) have all been considered at one time to be among the first exoplanets likely to host habitable environments if they were rocky (*2*, *7*, *14*, *15*), with d still being considered an excellent candidate. This system continues to be studied intensively [e.g., (*16*)]. Because stellar activity is an important source of noise at the RV amplitudes of the GJ 581 planets, we seek herein to investigate the effects of stellar activity on the RVs of GJ 581 in more detail.

[1]Department of Astronomy and Astrophysics, The Pennsylvania State University, University Park, PA 16802, USA. [2]Center for Exoplanets and Habitable Worlds, The Pennsylvania State University, University Park, PA 16802, USA. [3]The Penn State Astrobiology Research Center, The Pennsylvania State University, University Park, PA 16802, USA. [4]McDonald Observatory, The University of Texas at Austin, Austin, TX 78712–1206, USA.
*Corresponding author. E-mail: pmr19@psu.edu

Our analysis of correlation between the RVs and stellar activity indicators focuses on the publicly available spectra from the HARPS spectrograph (based on data obtained from the European Southern Observatory Science Archive Facility under request no. 58160). We adopted the newest published HARPS RVs (*8*) and measured activity indicators for the Hα ($I_{H\alpha}$) (*17*) and Na I D (I_D) (*18*) lines using the spectra. Using the cross-correlation functions (CCFs) included with the HARPS spectra, we have calculated the bisector inverse slopes (BIS) as well. We have excluded one spectrum from our analysis, because it is likely a flare event. Visual inspection of the spectra reveals that I_D is contaminated by strong night sky sodium emission lines, which are difficult to correct without sky fibers. We therefore constrained our RV analysis to Hα to minimize error.

The RVs of GJ 581 are dominated by the signal of planet b. Upon removing this dominant signal, we detect significant anticorrelation in the RV residuals with $I_{H\alpha}$. For the entire data set (239 spectra), the Pearson correlation coefficient is $r = -0.31$ [probability of no correlation, $P(r) = 5 \times 10^{-7}$]. Examining the BIS for the HARPS data, we also see evidence for a correlation ($r = 0.44$ over the most active period) between BIS and $I_{H\alpha}$, as might be expected if stellar activity is the cause of some RV shifts for GJ 581 (fig. S10).

Frequency analysis of the activity indices indicates that their variability—and thus the induced RV signal—is associated with stellar rotation (fig. S1). The periodogram of $I_{H\alpha}$ shows a strong peak at 125 days, with an additional peak at 138 days caused by phase changes in the rotation signal. The best fit to the time-series $I_{H\alpha}$ data is obtained when we model individual sinusoids to the periods from December 2005 to September 2007 and January 2010 to July 2011, when the $I_{H\alpha}$ root mean square (RMS) is twice

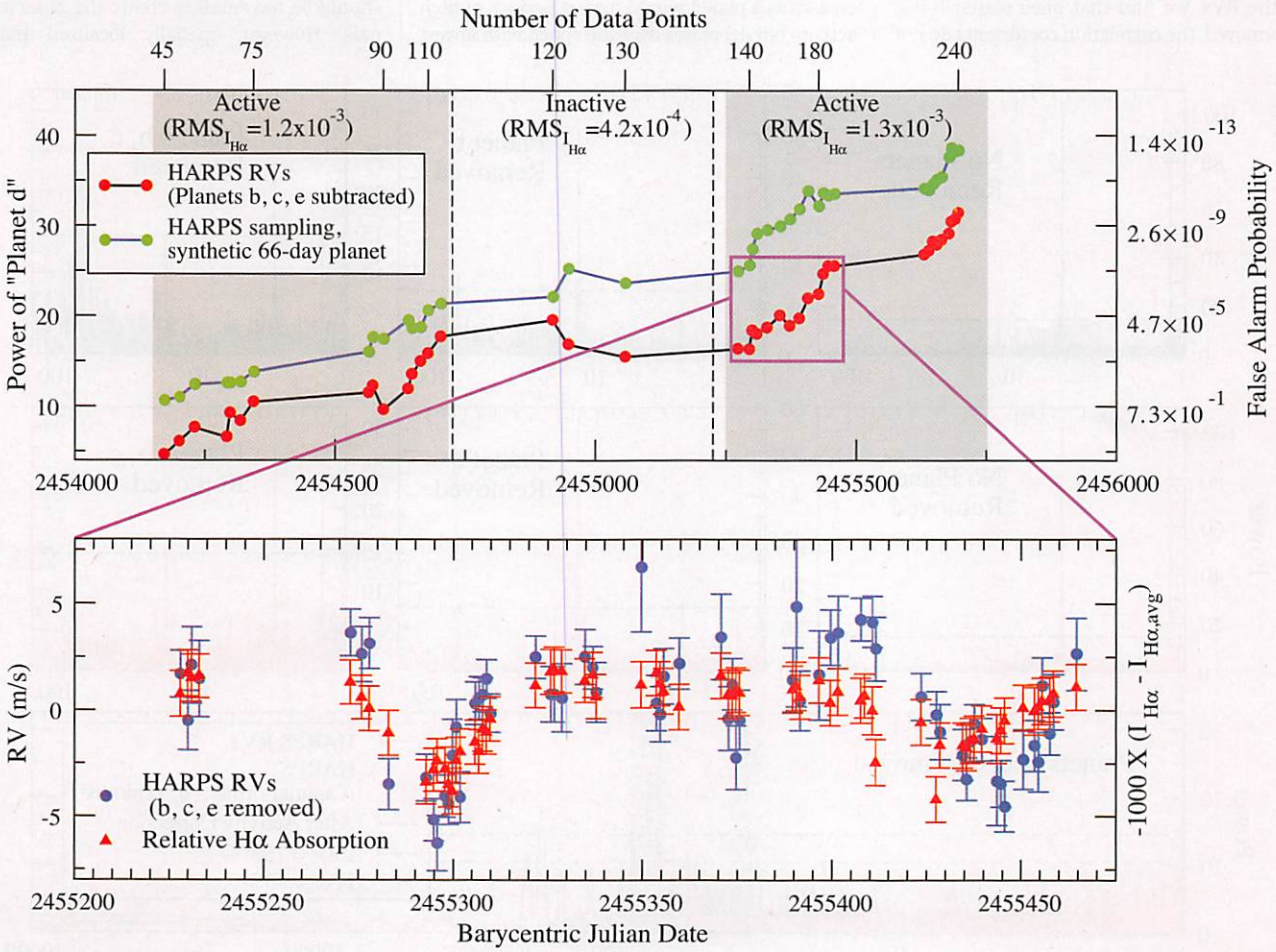

Fig. 1. (**Top**) Periodogram power of d as a function of time and number of HARPS RVs. The power is reported at every five observations. We show the actual RVs after removing planets b, c, and e (black/red), along with the Keplerian signal of an eccentric 66-day planet sampled with the time stamps and uncertainties of the HARPS sampling (blue/green). Qualitative levels of stellar activity, based on the $I_{H\alpha}$ index, are shown for different time periods. (**Bottom**) HARPS RVs (blue) for the region outlined in pink. Planets b, c, and e have been modeled and removed from the RVs. We overlay our Hα index (red), scaled to facilitate visual comparison. RV and Hα are strongly correlated, indicating that the remaining Doppler signal is caused by stellar activity.

as high as during the "quiescent" periods in 2005 and 2009. The sinusoidal models yield an average rotation period of 130 ± 2 days, whereas the phase and (to a lesser extent) amplitude vary.

The changing phase and amplitude of the activity-induced stellar rotation signal induce a variable effect on the RVs, implying that the slope of the RV-activity correlation is not strictly constant. Instead of evaluating the RV-activity correlation as one fit over the entire data set, we have examined RV as a function of $I_{H\alpha}$ over each observing season in the HARPS archive. For the December 2005 to September 2007 and January 2010 to July 2011 time frames, we have combined two seasons, because $I_{H\alpha}$ shows a coherent rotation signal across the seasons, suggesting that the activity behavior remains approximately constant over these times.

We find significant RV-$I_{H\alpha}$ anticorrelations (r = −0.45, −0.55, and −0.48) for three of the five epochs. These three epochs have RMS values of 1.22×10^{-3}, 1.10×10^{-3}, and 1.31×10^{-3} in $I_{H\alpha}$, as opposed to $RMS_{IH\alpha} = 4.81 \times 10^{-4}$ and 4.19×10^{-4} in the other seasons, suggesting that the star is approximately twice as active during these times. Although we have removed planets b, c, and e from the RVs, we find that once planet b has been removed, the correlation coefficients do not change significantly before and after removing c and e. The anticorrelation is particularly striking for the 2010 season, shown in Fig. 1.

We correct the HARPS RVs by subtracting the best-fit RV-$I_{H\alpha}$ relation from each of the three epochs for which we observed a significant anticorrelation, leaving the other epochs unchanged. A new RV model then can be used to evaluate the effect of the activity correction on the known exoplanets and to determine whether any additional signals exist. We detect the known planets b, c, and e using the generalized Lomb-Scargle periodogram (*19*) (Fig. 2). For planets c and e, we observe significant increases in signal power upon correcting for activity. The power of planet c increases from 53.5 to 57.6, while the power of e increases from 23.5 to 30.3. Formally, false-alarm probability (FAP) [from (*11*)] scales approximately as $e^{-P}\sqrt{P}$ for a Lomb-Scargle periodogram with power P; thus, the power increase translates to a decrease in FAP by a factor of 60 for planet c and 800 for planet e.

In contrast, the power of planet d drops from 31.4 to 11.6 after we apply our activity correction. As shown in Fig. 1, the periodogram power increases as a planet would during periods of high activity but decreases over the epoch with lowest $RMS_{IH\alpha}$. Planet d has a reported period of 66 days, which is roughly equal to half the stellar rotation period, suggesting that it is a harmonic that loses significance when the rotation signal is removed via decorrelating with $I_{H\alpha}$.

In Table 1, we list the parameters of our three-planet model to the activity-corrected HARPS RVs. We fit the RVs using the GaussFit (*20*) and Systemic (*21*) software packages, finding good agreement between the two. Our model does not differ much from previous fits to planets b, c, and e (*3*, *8*, *9*), except that planet e no longer shows any eccentricity after the activity correction. In the corrected RVs, the 66-day signal appears only at the 1.5-SD significance level in the residual periodogram, and the 33- or 36-day signal does not appear at all. We conclude that the three-planet solution with activity-induced variability fully explains the observations.

We assert that the periodic RV signal at 66 days is an artifact induced by the stellar rotation rather than an exoplanet. Previous studies (*3*, *7*) discounted starspot-induced rotational modulation as the origin of RV signals corresponding to planets d and g because the low photometric variability of the star suggests that any spots present should be too small to create the observed signals. However, spatially localized magnetic

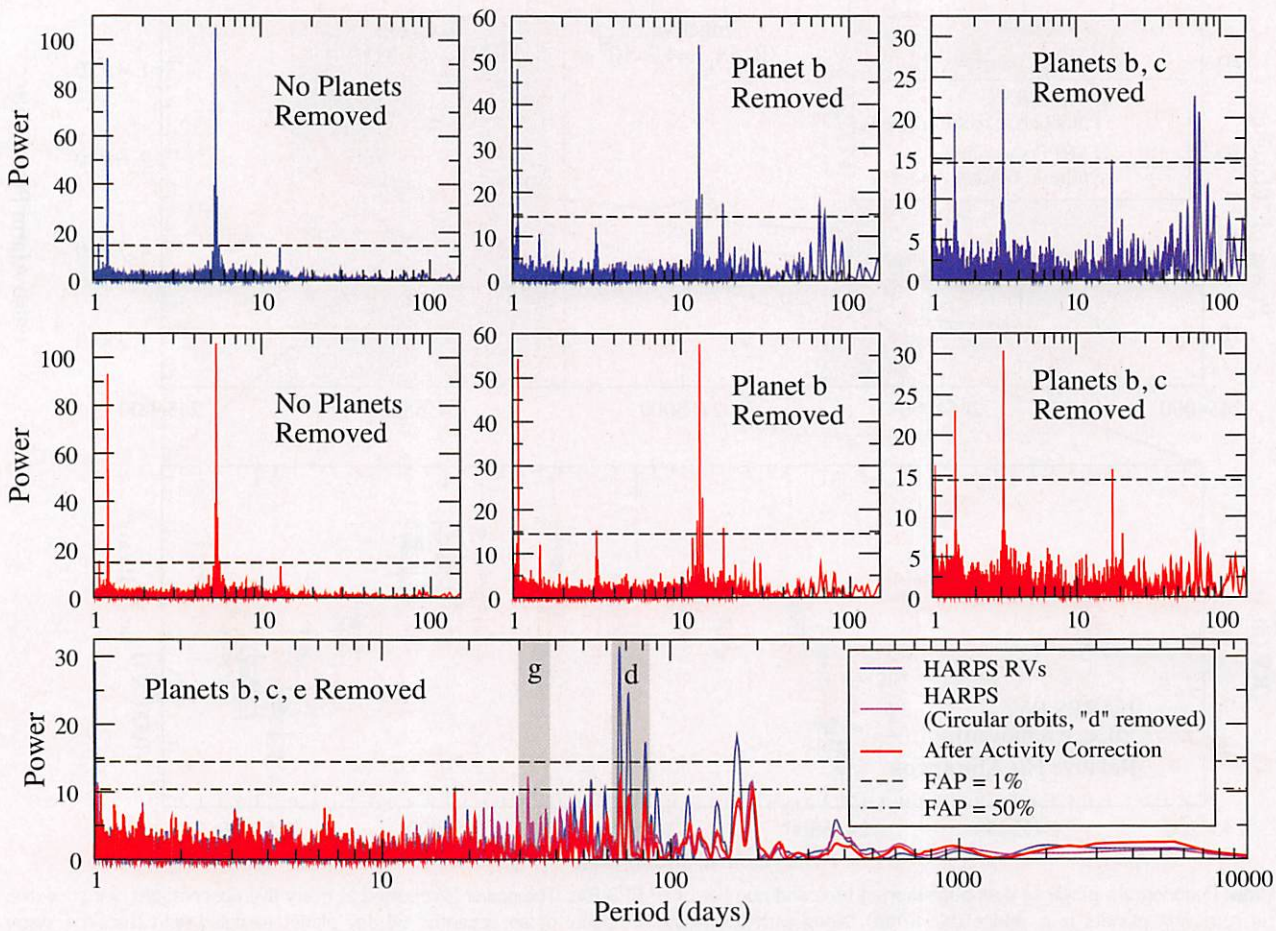

Fig. 2. Periodograms for the HARPS RVs before (blue) and after (red) correcting for stellar activity, with the planets successively subtracted. In the bottom panel, we also show (pink) the periodogram after subtracting four circular Keplerian signals, illustrating that the signal interpreted as 581 g (*7*, *9*) was caused by fitting a sinusoidal signal to the 581d signal and performing, in essence, an incomplete correction for stellar activity.

activity has been observed to influence RV in M stars without producing spots with high optical contrast. Striking similarities exist with our observed activity-RV correlation results for GJ 581 and those reported for Barnard's star, a slow-rotating, photometrically quiet M dwarf of similar spectral type. Observations with the Ultraviolet and Visual Echelle Spectrograph (UVES) found an RV-$I_{H\alpha}$ anticorrelation value of $r = -0.498$, almost identical to that observed herein (*22*). Kürster *et al.* attribute this phenomenon to magnetically active regions that stimulate Hα emission but do not produce spots of high contrast. These regions impede local convection, leading to an RV shift. Evidence for a relation between chromospheric activity, Hα emission, and convective suppression has also been observed in the form of a temperature/radius dependence on Hα activity for low-mass stars (*23*). The anticorrelation (i.e., the negative slope) for RV versus $I_{H\alpha}$ suggests that the stellar lines used for RV determination are emitted from a region of convective overshoot.

Although the activity-induced RV we observe may not be due to "typical" dark starspots, localized, rotating regions that magnetically alter the convective velocity field would create RV signatures equivalent to spots. In the absence of simultaneous high-precision photometric monitoring, it is difficult to deduce the relative contributions of these different mechanisms. We therefore refer to these as active regions (ARs) hereafter. A single rotating starspot creates an RV signal at the rotation period and injects power at a number of its harmonics, primarily $P_{rot}/2$, $P_{rot}/3$, and $P_{rot}/4$ (*24*). For the purposes of exploring the qualitative impact of such ARs on RV, a starspot model should suffice. For a rotation period of 130 days, the activity-induced RV signal always includes significant power near the period of planet d. We present two hypotheses for the lack of an observed signal at the periodogram around 130 days. One explanation lies in the geometry of the star and its ARs. The shape of an activity-induced RV signal changes as a function of the stellar inclination and the latitudes of the ARs, sometimes transferring RV power out of the rotation period into its harmonics. As an illustration, in an analysis using the SOAP (Spot Oscillation and Planet) code (*24*) (fig. S7), for an inclination of 50° for the star [consistent with that of its debris disk (*4*)] and spots near the stellar equator, the spot-induced RVs are dominated by the 66-day signal. A more important factor, though, is that for the 2010 to 2011 observing epoch, the Hα activity contains two signals of roughly equal power at 128 and 69 days, indicating the presence of two ARs instead of one. In this epoch, we find (fig. S4) that the activity-RV correlation is driven by the 69-day signal rather than the rotation period, indicating that activity is injecting RV power at half the rotation period while two ARs are present. The addition of power at half the rotation period for 109 of 240 observations explains the dominance of the $P_{rot}/2$ signal.

Our activity analysis also helps explain why the signal ascribed to planet d is not observed in the Keck/HIRES RVs alone (*11*). We have computed $I_{H\alpha}$ for the HIRES spectra, which we show alongside the HARPS measurements in Fig. 3. The HIRES data only cover the last portion of the active phase from December 2005 to September 2007 and have very little coverage in 2010 to 2011, where two ARs drive the 66-day period. Coupled with the higher reported error bars of HIRES compared with HARPS, this yields a non-detection of the 66-day signal.

The signal of the 33- or 36-day "planet g," the existence of which has already been called into question, is also an artifact of stellar rotation because no hint of it remains after the activity correction. Close to $P = P_{rot}/4$, it is another harmonic of the rotation period. Furthermore, the signal is only observed when fitting a circular orbit to "planet d," as shown in the bottom panel of Fig. 2 (*7*–*9*). By fitting a circular Keplerian model to the 66-day signal, Vogt *et al.* (*7*) essentially performed an incomplete stellar activity correction, and the signal of "planet g" was simply leftover noise created by stellar activity.

The impact of stellar activity on the GJ 581 system demonstrates the crucial importance of understanding and treating the presence of activity signals in the quest for low-mass planets. Our activity correction clearly distinguishes between planetary and stellar signals and reduces the astrophysical noise in the data sufficiently that the signals of very low-mass planets are recovered at much higher significance. This analysis also naturally explains the correlated (red) noise seen in analysis of the HARPS and HIRES data (*11*).

Given the advantages of RV surveys of slow-rotating low-mass M dwarfs for RV searches, the physical mechanism that inhibits the convective motion in the stellar atmosphere should be the

Table 1. Orbital solution for GJ 581 planets after correcting for stellar activity. AU, astronomical units; BJD, barycentric Julian date.

Orbital parameter	Planet b	Planet c	Planet e
Period P (days)	5.3686 ± 0.0001	12.914 ± 0.002	3.1490 ± 0.0002
Periastron passage T_0 (BJD −2,450,000)	4751.76 ± 0.01	4759.2 ± 0.1	4752.33 ± 0.05
RV amplitude K (m/s)	12.6 ± 0.2	3.3 ± 0.2	1.7 ± 0.2
Eccentricity e	0.00 ± 0.03	0.00 ± 0.06	0.00 ± 0.06
Semimajor axis a (AU)	0.04061 ± 0.00003	0.0721 ± 0.0003	0.02815 ± 0.00006
Minimum mass $M \sin i$ ($M_\oplus$)	15.8 ± 0.3	5.5 ± 0.3	1.7 ± 0.2
Zero-point RV offset (m/s)	−0.52 ± 0.1		
RMS (m/s)	2.12		

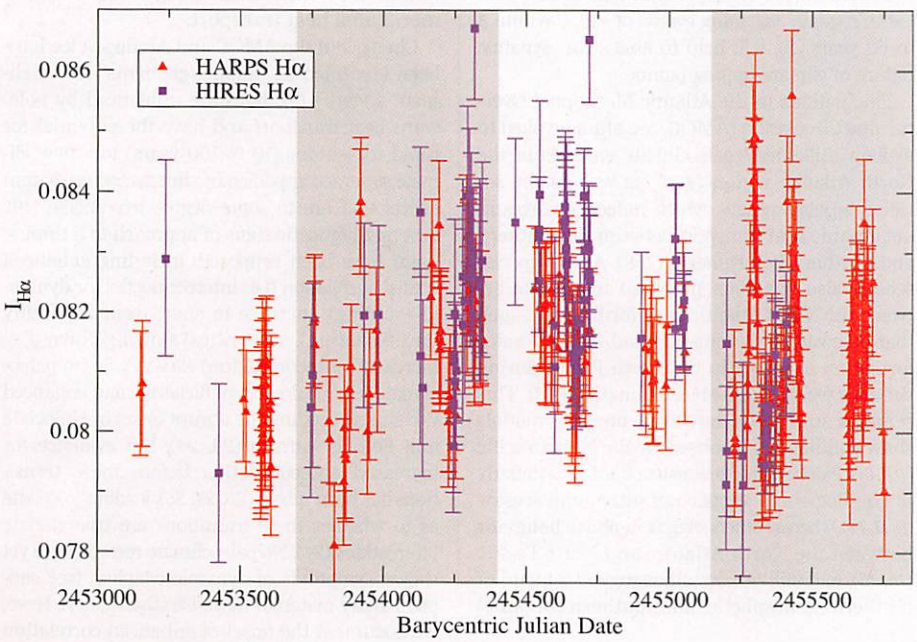

Fig. 3. Hα indices from HARPS (red) and HIRES (purple). The periods of greatest rotational modulation are shaded. Note the sparse HIRES coverage in the last shaded region, where the signal of the 66-day signal is strongest in both RV and $I_{H\alpha}$.

focus of additional scrutiny. Magnetic activity that impedes the local convective velocity in solar-type stars is invariably accompanied by a dark starspot, so the low contrast of spots in the ARs of Barnard's star and GJ 581 may be a feature unique to low-mass stars. More robust theoretical modeling of magnetohydrodynamics in the atmospheres of old, low-mass stars is required to fully understand this phenomenon.

GJ 581d and (the now less widely believed to exist) GJ 581 g were considered to be among the first exoplanets likely to host habitable environments if they were rocky (*7*, *15*). Given the small number of habitable-zone (HZ) (*25*) planets discovered by Doppler surveys around M dwarfs, the removal of GJ 581d affects the RV-based estimate of $\eta_\oplus$ (the fraction of stars hosting low-mass planets in their HZs) around M stars. This has been estimated as $\eta_\oplus = 0.41^{+0.54}_{-0.13}$ by the HARPS M dwarf survey (*26*). The exclusion of GJ 581d reduces the rate to 33%, still within the stated error limits. More precise estimates of $\eta_\oplus$ for M stars from Kepler exist [e.g., (*5*)], but the various HZ limits used by these estimates prevent direct comparison. Although GJ 581 may still be dynamically capable of accommodating terrestrial-mass planets in its HZ, we see no evidence at this time for additional planets in the activity-corrected residuals around our three-planet model.

REFERENCES AND NOTES

1. X. Bonfils *et al.*, *Astron. Astrophys.* **443**, L15–L18 (2005).
2. S. Udry *et al.*, *Astron. Astrophys.* **469**, L43–L47 (2007).
3. M. Mayor *et al.*, *Astron. Astrophys.* **507**, 487–494 (2009).
4. J.-F. Lestrade *et al.*, *Astron. Astrophys.* **548**, A86 (2012).
5. C. D. Dressing, D. Charbonneau, *Astrophys. J.* **767**, 95 (2013).
6. R. K. Kopparapu, *Astrophys. J. Lett.* **767**, L8 (2013).
7. S. S. Vogt *et al.*, *Astrophys. J.* **723**, 954–965 (2010).
8. T. Forveille *et al.*, ArXiv 1109.2505 (2011); http://arxiv.org/abs/1109.2505.
9. S. S. Vogt, R. P. Butler, N. Haghighipour, *Astron. Nachr.* **333**, 561–575 (2012).
10. P. C. Gregory, *Mon. Not. R. Astron. Soc.* **415**, 2523–2545 (2011).
11. R. V. Baluev, *Mon. Not. R. Astron. Soc.* **429**, 2052–2068 (2013).
12. A. P. Hatzes, *Astron. Nachr.* **334**, 616–624 (2013).
13. M. Tadeu dos Santos, G. G. Silva, S. Ferraz-Mello, T. A. Michtchenko, *Celestial Mech. Dyn. Astron.* **113**, 49–62 (2012).
14. F. Selsis *et al.*, *Astron. Astrophys.* **476**, 1373–1387 (2007).
15. R. D. Wordsworth *et al.*, *Astrophys. J. Lett.* **733**, L48 (2011).
16. D. A. Joiner, C. Sul, D. Dragomir, S. R. Kane, M. E. Kress, *Astrophys. J.*, ArXiv 1404.4381 (2014).
17. P. Robertson, M. Endl, W. D. Cochran, S. E. Dodson-Robinson, *Astrophys. J.* **764**, 3 (2013).
18. R. F. Díaz, C. Cincunegui, P. J. D. Mauas, *Mon. Not. R. Astron. Soc.* **378**, 1007–1018 (2007).
19. M. Zechmeister, M. Kürster, *Astron. Astrophys.* **496**, 577–584 (2009).
20. W. H. Jefferys, M. J. Fitzpatrick, B. E. McArthur, *Celestial Mech.* **41**, 39–49 (1988).
21. S. Meschiari *et al.*, *Publ. Astron. Soc. Pac.* **121**, 1016–1027 (2009).
22. M. Kürster *et al.*, *Astron. Astrophys.* **403**, 1077–1087 (2003).
23. K. G. Stassun, K. M. Kratter, A. Scholz, T. J. Dupuy, *Astrophys. J.* **756**, 47 (2012).
24. I. Boisse, X. Bonfils, N. C. Santos, *Astron. Astrophys.* **545**, A109 (2012).
25. R. K. Kopparapu *et al.*, *Astrophys. J.* **765**, 131 (2013).
26. X. Bonfils *et al.*, *Astron. Astrophys.* **549**, A109 (2013).

ACKNOWLEDGMENTS

We acknowledge support from NSF grants AST-1006676, AST-1126413, AST-1310885, The Penn State Astrobiology Research Center, and the NASA Astrobiology Institute (NNA09DA76A) in our pursuit of precise RVs in the near infrared. This work was supported by funding from the Center for Exoplanets and Habitable Worlds. The Center for Exoplanets and Habitable Worlds is supported by the Pennsylvania State University, the Eberly College of Science, and the Pennsylvania Space Grant Consortium. M.E. is supported by NASA through the Origins of Solar Systems Program grant NNX09AB30G and grant AST-1313075 from the NSF. This research has made use of the Keck Observatory Archive (KOA), which is operated by the W. M. Keck Observatory and the NASA Exoplanet Science Institute (NExScI), under contract with the National Aeronautics and Space Administration. We thank C. Bender for assistance in studying telluric absorption in the vicinity of Hα. The data produced for this study are included in table S3 of the supplementary materials.

SUPPLEMENTARY MATERIALS

www.sciencemag.org/content/345/6195/440/suppl/DC1
Materials and Methods
Figs. S1 to S10
Tables S1 to S3
References (*27*–*32*)

12 March 2014; accepted 17 June 2014
Published online 3 July 2014;
10.1126/science.1253253

PALEOCLIMATE

Synchronization of North Pacific and Greenland climates preceded abrupt deglacial warming

Summer K. Praetorius* and Alan C. Mix

Some proposed mechanisms for transmission of major climate change events between the North Pacific and North Atlantic predict opposing patterns of variations; others suggest synchronization. Resolving this conflict has implications for regulation of poleward heat transport and global climate change. New multidecadal-resolution foraminiferal oxygen isotope records from the Gulf of Alaska (GOA) reveal sudden shifts between intervals of synchroneity and asynchroneity with the North Greenland Ice Core Project (NGRIP) $\delta^{18}O$ record over the past 18,000 years. Synchronization of these regions occurred 15,500 to 11,000 years ago, just prior to and throughout the most abrupt climate transitions of the last 20,000 years, suggesting that dynamic coupling of North Pacific and North Atlantic climates may lead to critical transitions in Earth's climate system.

Abrupt climate transitions observed during the last deglaciation (*1*, *2*) and within the last glacial interval (*3*) demonstrate that internal climate feedbacks can amplify the effects of relatively weak external climate forcing. Understanding the mechanisms involved in generating past abrupt transitions, which have led to regional warming events of ~10°C within 3 to 60 years (*2*), will help to assess the dynamic nature of climate tipping points.

Fluctuations in the Atlantic Meridional Overturning Circulation (AMOC) are often invoked to explain millennial-scale climate changes in the North Atlantic region (*4*–*6*), as well as the so-called bipolar seesaw, which reflects changes in net oceanic heat transport between the southern and northern hemispheres (*7*, *8*). An interocean seesaw also has been proposed to operate between the North Atlantic and North Pacific, such that poleward heat transport and/or deep-water formation increases in the North Pacific during times of weakened AMOC strength (*9*–*11*). This remains uncertain, however, because models show conflicting responses for the North Pacific (*10*–*13*). Paleoclimate reconstructions are similarly in conflict; some support an interocean seesaw (*9*, *11*, *14*), whereas others suggest in-phase behavior between the North Atlantic and North Pacific (*15*, *16*), and still other studies suggest a blend of northern (atmospheric) and southern (oceanic) influences (*17*, *18*). If an Atlantic-Pacific seesaw exists, low northward heat transport in one ocean might be partly compensated by high northward heat transport in the other. Conversely, synchronous variations in the two oceans would tend to amplify climate changes in the high northern latitudes by either enhancing or diminishing meridional heat transport.

Changes in the AMOC and Arctic sea ice have been identified as "tipping elements" in the climate system (*19*); both are influenced by poleward heat transport and have the potential for rapid transitions (10 to 100 years) to a new climate state, accompanied by climate and ecosystem effects that are to some degree irreversible (*19*). Several diagnostic signs of approach to a tipping point have been proposed, including enhanced spatial correlation (i.e., interconnection or dynamic coupling), increase in short-term variability (i.e., flickering), and critical slowing down (i.e., increased autocorrelation) (*20*–*22*). Some paleoclimate records document flickering and enhanced variance preceding the abrupt onset of Holocene and Bølling warmth (*23*, *24*), but evidence for increased autocorrelation before these transitions has been mixed (*20*, *24*, *25*), leading to debate as to whether these transitions are true climate bifurcations (*24*). No paleoclimate records have yet shown symptoms of dynamic coupling (see supplementary materials for illustrative model). Here, we document the onset of enhanced correlation between North Pacific and North Atlantic climate variability that shortly precedes the most abrupt warming events of the last deglaciation.

College of Earth, Ocean, and Atmospheric Sciences, Oregon State University, Corvallis, OR 97331, USA.
*Corresponding author: E-mail: spraetor@coas.oregonstate.edu